PAPER • OPEN ACCESS

Spatially-resolved UV-C emission in epitaxial monolayer boron nitride

View the article online for updates and enhancements.

2D Materials

Spatially-resolved UV-C emission in epitaxial monolayer boron nitride

A Rousseau[1], J Plo[1], P Valvin[1], T S Cheng[2], J Bradford[2] [iD], T S S James[2] [iD], J Wrigley[2], C J Mellor[2] [iD], P H Beton[2] [iD], S V Novikov[2,*] [iD], V Jacques[1], B Gil[1] [iD] and G Cassabois[1,3,*] [iD]

[1] Laboratoire Charles Coulomb UMR 5221 CNRS-Université de Montpellier, 34095 Montpellier, France
[2] School of Physics and Astronomy, University of Nottingham, Nottingham NG7 2RD, United Kingdom
[3] Institut Universitaire de France, 75231 Paris, France
* Authors to whom any correspondence should be addressed.

E-mail: sergei.novikov@nottingham.ac.uk and guillaume.cassabois@umontpellier.fr

Abstract

We report hyperspectral imaging in the UV-C spectral domain in epitaxial monolayers of hexagonal boron nitride (hBN). Under quasi-resonant laser excitation, the UV-C emission of monolayer hBN consists in resonant Raman scattering and photoluminescence, which appear to be spatially uncorrelated. Systematic measurements as a function of the excitation energy bring evidence of a photoluminescence singlet at ∼6.045 eV. The spatial variations of the photoluminescence energy are found to be around ∼10 meV, revealing that the inhomogeneous broadening is lower than the average photoluminescence linewidth of ∼25 meV, a value close to the radiative limit in monolayer hBN. Our methodology provides an accurate framework for assessing the opto-electronic properties of hBN in the prospect of scalable hBN-based devices fabricated by epitaxy.

Hexagonal boron nitride (hBN) is a pivotal crystal in the family of 2D materials [1, 2]. In its bulk form, the electronic bandgap of hBN is calculated to be indirect at around 6 eV [3–5]. Experimental evidence for indirect-gap bulk hBN was brought by optical spectroscopy in the UV-C spectral range [6–10], and independently confirmed by electron energy loss spectroscopy [11]. The suppression of any interlayer coupling in the limit of atomically-thin hBN induces a subtle shift of the conduction band minimum, that makes monolayer hBN a direct-gap semiconductor [3–5]. The indirect-direct crossover of the bandgap was first experimentally demonstrated in hBN, not by microscopy in samples fabricated by exfoliation of bulk lamellar crystals as in transition metal dichalcogenides [12, 13], but by reflectivity and photoluminescence (PL) spectroscopy in large-scale monolayer hBN epitaxially grown on graphite by high-temperature molecular beam epitaxy (HT-MBE) [14]. This disparity between transition metal dichalcogenides and hBN stemmed from the technical difficulties related to performing optical microscopy in the UV-C spectral range.

Recently, we reported hyperspectral imaging in exfoliated hBN flakes at low temperature [15], by means of a scanning confocal cryomicroscope operating at the diffraction limit at wavelengths around 200 nm [16]. Emission slightly above 6 eV was specifically detected in atomically-thin hBN but not in multilayer hBN [15], thus confirming, in exfoliated hBN flakes, the direct-bandgap crossover initially observed in epitaxial monolayer hBN [14]. Beyond the reproducible evidence of direct-gap monolayer hBN in epitaxial and exfoliated samples, PL spectroscopy emerges as the preferential characterization tool to resolve the emission of atomically-thin hBN, cathodoluminescence being of limited use because of intrinsic limitations in the limit of ultrathin crystals [17, 18].

A specific issue with PL in monolayer hBN arises from the huge excitonic binding energy, which is calculated to be ∼2 eV in suspended monolayer hBN [19]. Although this value is reduced by ∼1 eV for monolayer hBN on graphite because of the screening of the Coulomb interaction induced by the substrate [20], the onset of the continuum absorption still lies at ∼7 eV (λ ∼ 175 nm), an energy corresponding to the vacuum UV spectral domain, beyond the reach of any tabletop laser. This prevents the photogeneration of free electron–hole pair states

in the absorption continuum of monolayer hBN, so that a quasi-resonant excitation via phonon-assisted processes is required [14, 21]. Such configuration leads to the coexistence of resonant Raman scattering and PL [14, 15, 22], which in turn complicates the interpretation of optical spectroscopy when characterizing atomically-thin hBN in the UV-C range.

Here we report hyperspectral imaging in the UV-C spectral domain in epitaxial monolayer hBN, under quasi-resonant laser excitation. Our sample consists of atomically-thin hBN expitaxially grown by HT-MBE on highly oriented pyrolytic graphite (HOPG) in conditions where hBN partially covers the graphite substrate. Thanks to our spatially-resolved measurements of the UV-C emission, we spatially isolate the distinctive contributions of resonant Raman scattering and PL. We provide a quantitative interpretation of our experiments by means of a weighted average of resonant Raman scattering and PL, from which we extract the maps of their respective amplitudes in our epitaxial monolayer hBN sample. No spatial correlation of the resonant Raman scattering and PL amplitudes is observed. The PL signal consists in a singlet at ∼6.045 eV, with spatial variations of the PL energy around ∼10 meV, thus revealing that the inhomogeneous broadening is lower than the average PL linewidth of ∼25 meV, a value close to the radiative limit determined by reflectivity experiments [23]. Our methodology provides an accurate framework for assessing the opto-electronic properties of hBN in the prospect of scalable hBN-based devices fabricated by epitaxy.

We have developed HT-MBE for the growth of hBN layers on HOPG at temperatures from 1250 °C, to 1700 °C, [14, 23–25]. We have used a high-temperature effusion Knudsen cell to provide a boron flux and RF plasma source to produce a flux of active nitrogen. We have demonstrated that by growing hBN on HOPG substrates at these extremely high temperatures it is possible to produce monolayer thick hBN with atomically-flat surfaces. The hBN coverage can be reproducibly controlled by the growth time, substrate temperature and boron to nitrogen flux ratios. The majority of the hBN monolayers is nucleated at HOPG step edges, but there are also some hBN islands nucleated on the HOPG terraces. With increase of the growth time the hBN monolayers gradually increase in size in a step-flow growth mode. The decrease of aggregates at higher growth temperatures reduces the available nucleation sites for a potential second hBN monolayer, therefore improving the viability of HT-MBE for the formation of atomically-flat single hBN monolayers without multilayer hBN regions. hBN coverage, hBN monolayer island shape and the presence of hBN aggregates can be controlled in HT-MBE with the highest quality hBN monolayers grown at a substrate temperature of about 1390 °C, [23, 25].
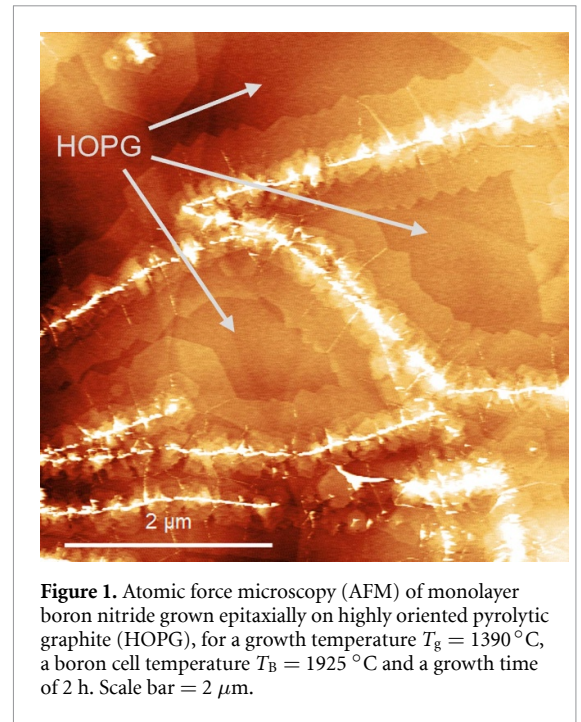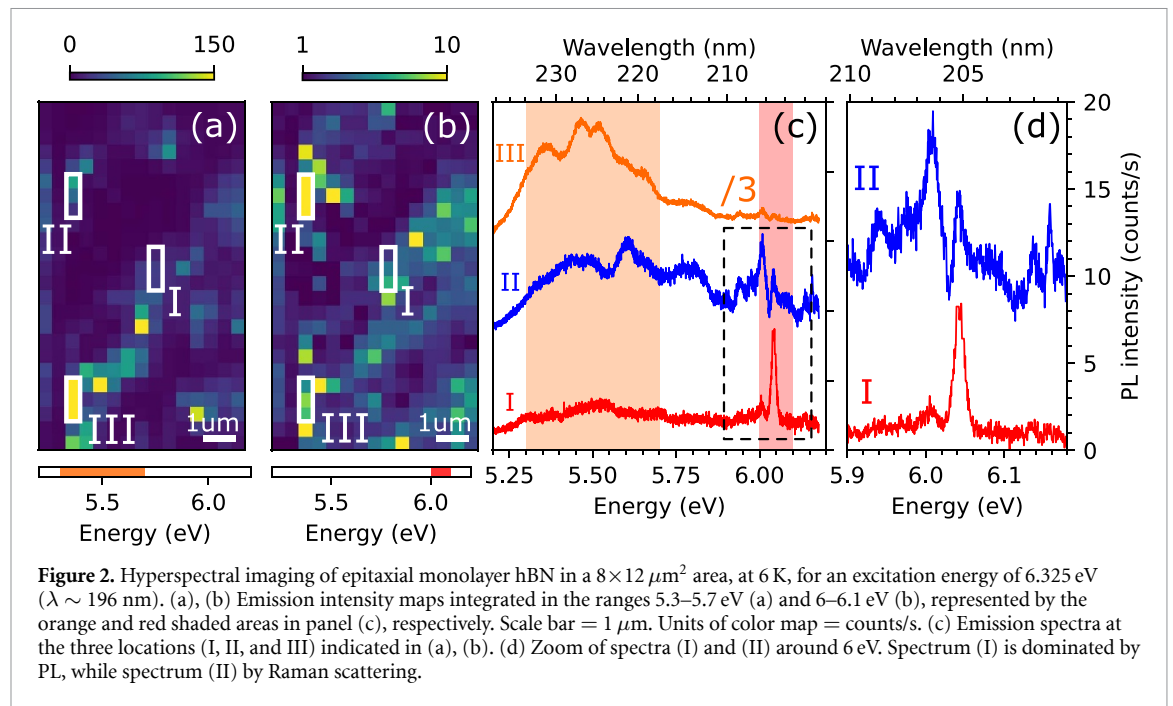

Figure 1. Atomic force microscopy (AFM) of monolayer boron nitride grown epitaxially on highly oriented pyrolytic graphite (HOPG), for a growth temperature $T_g = 1390\,°C$, a boron cell temperature $T_B = 1925\,°C$ and a growth time of 2 h. Scale bar = 2 μm.

Therefore, the hBN sample investigated in this paper was grown at about 1390 °C, using a fixed RF power of 550 W and a nitrogen flow rate of 2 sccm.

After HT-MBE growth the samples are removed from the system to allow the acquisition of atomic force microscopy (AFM) images of the surface (figure 1). Tapping mode AFM images were acquired using an Asylum Research Cypher-S instrument with NuNano Scout 70 probes. Distinguishing between materials is primarily achieved using the phase channel. All images were then processed with the Gwyddion software package [26].

The UV-C emission of monolayer hBN epitaxially grown on HOPG is analyzed by hyperspectral imaging with the scanning confocal cryomicroscope described in [16]. Briefly, the sample held at 6 K is excited by the fourth harmonic of a cw mode-locked Ti:Sa oscillator, tuned at a wavelength of 196 nm ($E_{ex} = 6.325$ eV) for the measurements displayed in figure 2. At each point of the $8 \times 12\ \mu$m^2 studied area (which is different from the one characterized in figure 1), the emission spectrum is recorded over a 30 nm-wide wavelength range centered at 220 nm, with an acquisition time of 60 s at an excitation power of 90 μW. Figure 2(a) displays the spatial variations of the emission intensity integrated between 5.3 and 5.7 eV, as indicated by the orange shaded area at the bottom of panel (a), and in panel (c) of figure 2. This spectral region corresponds to the recombination of excitons localized at hBN extended defects and stacking faults [15, 27, 28]. In contrast, figure 2(b) is the map of the intrinsic emission integrated between 6 and 6.1 eV (red shaded area at

Figure 2. Hyperspectral imaging of epitaxial monolayer hBN in a $8 \times 12 \ \mu m^2$ area, at 6 K, for an excitation energy of 6.325 eV ($\lambda \sim 196$ nm). (a), (b) Emission intensity maps integrated in the ranges 5.3–5.7 eV (a) and 6–6.1 eV (b), represented by the orange and red shaded areas in panel (c), respectively. Scale bar = 1 μm. Units of color map = counts/s. (c) Emission spectra at the three locations (I, II, and III) indicated in (a), (b). (d) Zoom of spectra (I) and (II) around 6 eV. Spectrum (I) is dominated by PL, while spectrum (II) by Raman scattering.

the bottom of panel (b), and in panel (c)), following previous studies pointing out the optical response of direct-gap monolayer hBN in this specific energy range [14, 15]. Representative emission spectra detected at three different points marked in panels (a) and (b) are plotted in figure 2(c), with a zoom around 6 eV for spectra (I) and (II) in figure 2(d).

The intensity maps in figures 2(a) and (b) are non-uniform with a signal globally distributed along diagonal lines, that may follow HOPG step-edges. No signal is detected in a $\sim$20 μm^2 region located between markers (I) and (II), neither for the defect-related PL (figure 2(a)), nor for the intrinsic emission (figure 2(b)). Given the $\sim$75% surface coverage of atomically-thin hBN determined by AFM in this sample, we thus attribute this dark regions to uncovered HOPG in figure 2. In figure 2(a) the spatial distribution of the defect-related luminescence is particularly inhomogeneous, with hot spots along lines parallel to the borders of uncovered HOPG. A typical spectrum recorded at position (III) illustrates the carrier relaxation in the presence of extended defects, with the usual broad luminescence band centered at $\sim$5.5 eV that completely dominates the emission spectrum at the hBN band-edge [27, 28]. A comparison of the spatially-resolved map of photogenerated excitons and our typical AFM images indicates that emission occurs from regions close to the edges of the atomically-thin hBN domains of epitaxially-grown material. Specifically we associate the spectra with a dominant peak at $\sim$6 eV as arising from monolayer hBN (consistent with the hyperspectral map discussed below), while the more disordered, multilayer hBN (corresponding to the bright linear structure in our AFM images) accounts for the more complex emission shown in figure 2 for regions II and III.

Excluding the region attributed to uncovered HOPG, the signal at $\sim$6 eV has a more uniform spatial distribution (figure 2(b)) than the defect-related PL (figure 2(a)), as could be expected from the intrinsic optical response of free excitons arising from monolayer hBN domains with a morphology similar to that in figure 1 [15, 27]. Nevertheless, one still observes some hot spots in figure 2(b). Interestingly, there are significant modifications of the emission spectrum within the recorded map, with two limit cases illustrated by spectra (I) and (II) recorded at the positions indicated in panels (a) and (b) of figure 2. The latter corresponds to a hot spot of figure 2(b), and spectrum (II) displays a complex multiplet structure. In contrast, a single line centered at $\sim$6.04 eV is detected at position (I). We will demonstrate below that spectrum (II) stems from resonant Raman scattering, while spectrum (I) is the genuine PL response of monolayer hBN.

A straightforward test to discriminate Raman scattering and PL consists in tuning the laser excitation energy. Under quasi-resonant excitation conditions, both Raman scattering and PL increase in intensity but the PL spectrum remains unchanged while the coherent Raman signal continuously shifts with the excitation energy, in other words, the Raman scattering spectrum is identical when plotted as a function of the detuning with the laser energy, the so-called Raman shift. This standard phenomenology in semiconductor optics [29] was recently reported in transition metal dichalcogenides monolayers [21]. The interplay between resonant Raman scattering and PL governs the UV-C emission of monolayer hBN as well. As explained in the introduction, this comes from the required quasi-resonant excitation to photo-generate excitons with a binding energy of
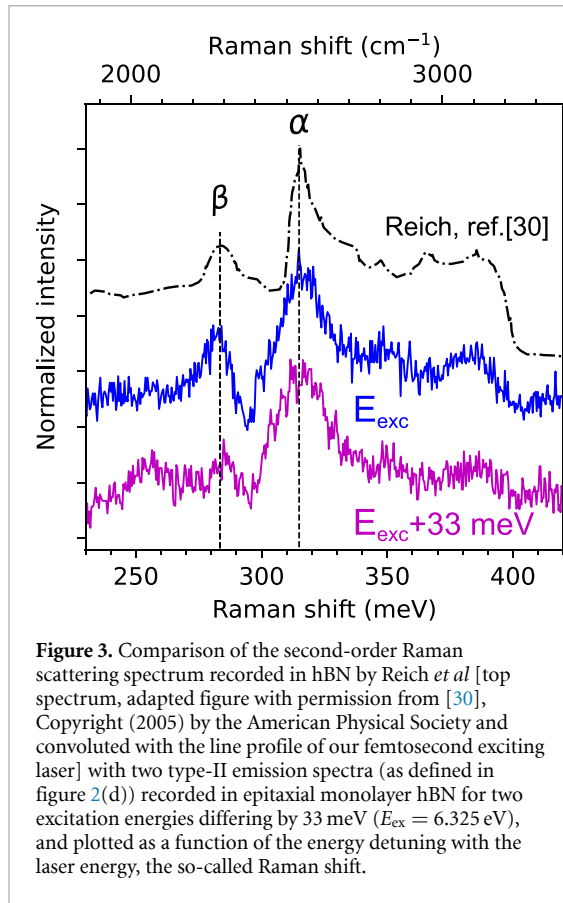
Figure 3. Comparison of the second-order Raman scattering spectrum recorded in hBN by Reich *et al* [top spectrum, adapted figure with permission from [30], Copyright (2005) by the American Physical Society and convoluted with the line profile of our femtosecond exciting laser] with two type-II emission spectra (as defined in figure 2(d)) recorded in epitaxial monolayer hBN for two excitation energies differing by 33 meV ($E_{\mathrm{ex}} = 6.325\,\mathrm{eV}$), and plotted as a function of the energy detuning with the laser energy, the so-called Raman shift.
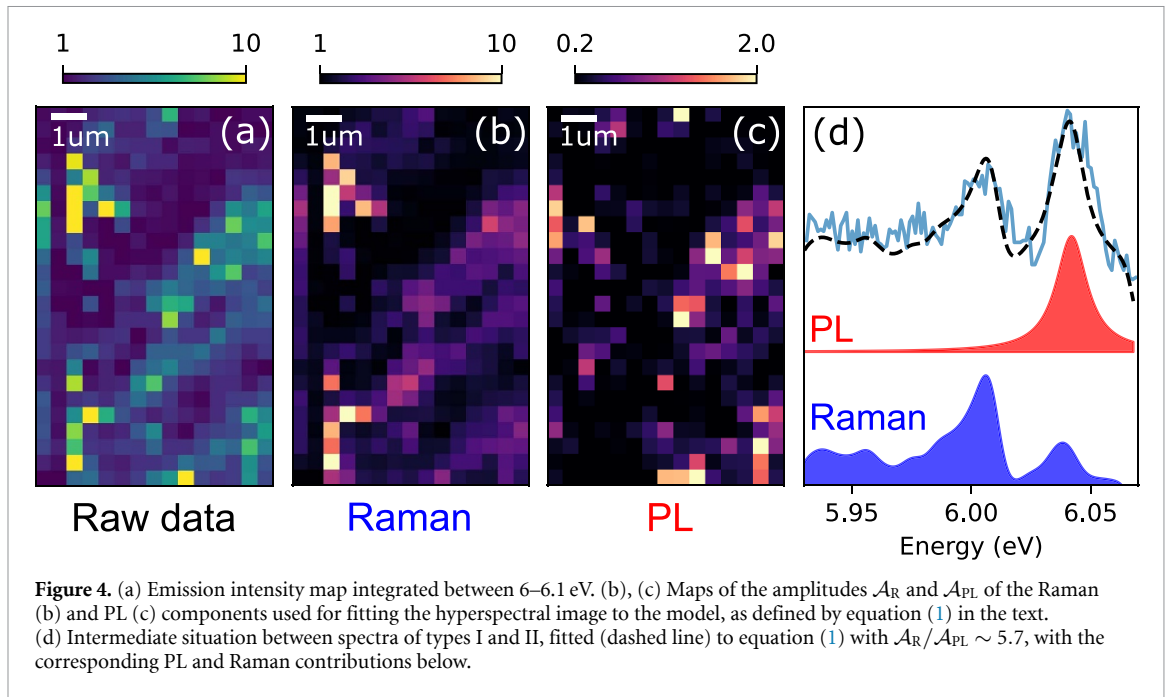
~1 eV in monolayer hBN on graphite [20]. Figure 3 displays two type-II spectra [as defined in figure 2], that are recorded for two different excitation energies, and plotted versus the Raman shift. The complex multiplet structure noted in figure 2 appears to be the same as a function of the Raman shift, thus demonstrating that the limit case of spectrum (II) in figure 2 is dominated by inelastic light scattering of the exciting laser. Importantly, these spectra exactly match the Raman scattering spectrum reported by Reich *et al* in [30] (dashed line, top spectrum in figure 3). In the present case of Raman shifts of the order of 300 meV (2500 cm^{-1}), the inelastic scattering signal corresponds to second-order Raman processes. The E_{2g} phonon mode of hBN at 170 meV (1370 cm^{-1}) gives rise to an intense Lorentzian line in the Raman scattering spectrum, that is accompanied by weak satellites at higher Raman shifts due to second-order processes mostly involving overtones of two identical phonons of opposite momenta [30]. In particular, the so-called α and β lines in figure 3 were attributed to the emission of two TO and two LA phonons, respectively [30].

The nature of spectrum (II) being identified, we perform a quantitative analysis of the data at each point (x, y) of the hyperspectral image, with a model based on a weighted average of Raman scattering and PL, following the equation:

$$\mathcal{A}_{\mathrm{R}}(x,y)\,\mathcal{F}(E - E_{\mathrm{ex}}) + \mathcal{A}_{\mathrm{PL}}(x,y)\,\mathcal{L}_{\Gamma(x,y)}(E - E_0(x,y))$$

$$(1)$$

where $\mathcal{F}(E - E_{\mathrm{ex}})$ is a normalized ad hoc function mimicking the second-order Raman spectrum of [30] [figure 3, top spectrum], and $\mathcal{L}_{\Gamma}(E - E_0)$ a normalized Lorentzian function centered at the energy E_0, with a full-width at half-maximum Γ. Therefore, spectra of type-I (type-II) correspond to $\mathcal{A}_{\mathrm{PL}} \gg \mathcal{A}_{\mathrm{R}}$ ($\mathcal{A}_{\mathrm{PL}} \ll \mathcal{A}_{\mathrm{R}}$, respectively). As seen in figure 4(d) showing an intermediate situation with comparable Raman and PL amplitudes ($\mathcal{A}_{\mathrm{R}}/\mathcal{A}_{\mathrm{PL}} \sim 5.7$), a fair agreement with the experimental data can be reached at any point of the sample with our model. The maps of the Raman ($\mathcal{A}_{\mathrm{R}}$) and PL ($\mathcal{A}_{\mathrm{PL}}$) amplitudes are displayed in figures 4(b) and (c), respectively, together with the raw data of the UV-C emission integrated between 6 and 6.1 eV in figure 4(a). There are hot spots in the $\mathcal{A}_{\mathrm{R}}$ map, where a roughly five-fold enhancement occurs at some points on the HOPG step-edges, with respect to the average Raman amplitude within monolayer hBN domains. Because these hot spots do not correlate with the ones of the defect-related PL in figure 2(a), they do not seem to be related to 3D islands preferentially nucleated at the HOPG step-edges. Moreover, despite similarities with the phenomenology of surface-enhanced Raman scattering where the electromagnetic field can be locally enhanced in surface irregularities acting as cavities, such an effect would augment both the Raman and PL amplitudes, which is not the case here when comparing figures 4(b) and (c). At the present stage, it is thus difficult to conclude on the origin of the Raman hot spots.
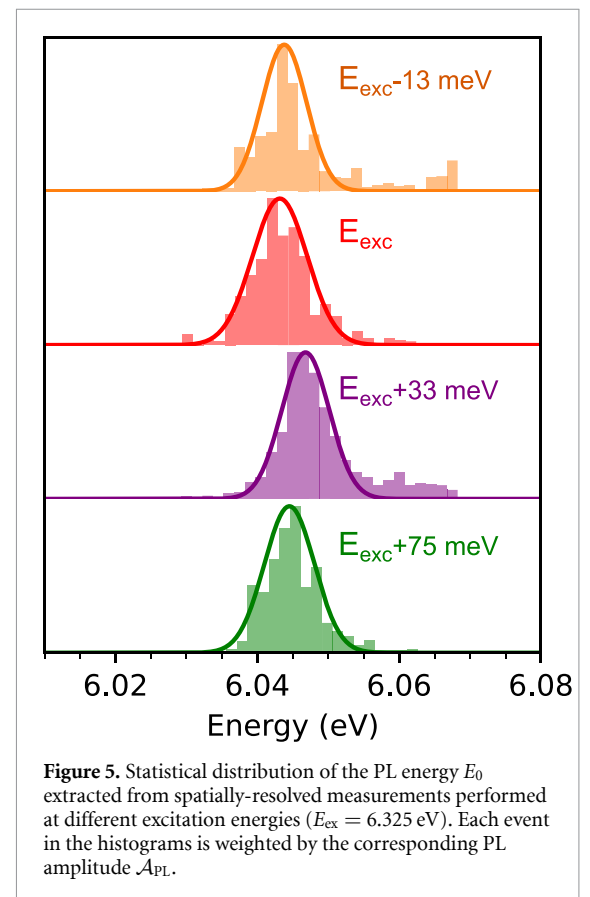
The PL amplitude $\mathcal{A}_{\mathrm{PL}}$ appears more homogeneously distributed, without any hot spot as for the Raman amplitude $\mathcal{A}_{\mathrm{R}}$ (figure 4(c)). Remarkably, there is almost no spatial correlation between the maps of the PL and Raman amplitudes, with a value of only 13% for the spatial covariance of $\mathcal{A}_{\mathrm{PL}}$ and $\mathcal{A}_{\mathrm{R}}$ normalized by the product of their standard deviations. Our quantitative analysis further resolves the spatial variations of the emission energy E_0 and linewidth Γ. The emission energy E_0 is peaked at ~6.045 eV with a standard deviation of 10 meV (figure 5). Importantly, this statistical distribution is unchanged when varying the excitation energy (figure 5), as expected for PL, thus validating *a posteriori* our framework of analysis based on a weighted average of Raman and PL. We highlight that the tuning range of the excitation energy in figure 5 is comparable to the spectral extension of the second-order Raman scattering signal (figure 3), meaning that the quasi-resonant excitation of the PL is performed via various two-phonon assisted processes in figure 5. Within this spectral range of excitation, the $\mathcal{A}_{\mathrm{PL}}/\mathcal{A}_{\mathrm{R}}$ ratio does not display any variations within our experimental uncertainties, with a constant value of ~0.2. The ~10 meV-variations of the PL energy in figure 5 reveal that the inhomogeneous broadening is lower than the average PL linewidth $\Gamma \sim 25$ meV (see for instance spectrum (I), figure 2(d)), a value close

Figure 4. (a) Emission intensity map integrated between 6–6.1 eV. (b), (c) Maps of the amplitudes $\mathcal{A}_R$ and $\mathcal{A}_{PL}$ of the Raman (b) and PL (c) components used for fitting the hyperspectral image to the model, as defined by equation (1) in the text. (d) Intermediate situation between spectra of types I and II, fitted (dashed line) to equation (1) with $\mathcal{A}_R/\mathcal{A}_{PL} \sim 5.7$, with the corresponding PL and Raman contributions below.

to the radiative limit in monolayer hBN [23]. This means that the PL signal can vary in amplitude from one point to another, but with little inhomogeneous broadening.

A major difference between the data of figure 5 and the ones of [14] recorded by macro-PL experiments in similar epitaxial monolayer hBN is the absence of a PL doublet in the present case. Previous PL measurements have indeed shown the existence of two lines at 6.05 and 6.08 eV [14]. This discrepancy may be related to the quasi-resonant excitation of the PL. More precisely, depending on the exact laser energy, one changes the overlap between the fixed PL line and the multiplet of second-order Raman scattering, that shifts with the laser energy, thus leading to an overall UV-C emission with a complex and non-universal spectrum. Although one can not exclude the existence of a PL doublet in the specific epitaxial monolayer hBN studied in [14], it is most likely that the reported doublet in [14] is not the intrinsic PL response of monolayer hBN, which was hidden by the superposition of the PL and Raman signals, with a spectrum of the latter more intricate than expected. The present systematic study by means of spatially-resolved measurements with different excitation energies allows to disentangle the contributions of Raman and PL, and brings the reproducible evidence of PL of monolayer hBN consisting in a singlet at $\sim$6.045 eV for hBN on graphite.

Eventually, we comment on the UV-C emission of exfoliated monolayer hBN reported in [15]. Following the same analysis procedure relying on the weighted average of Raman and PL defined in equation (1), a quantitative interpretation of the data in [15] is reached with $\mathcal{A}_R \sim 2.5\mathcal{A}_{PL}$, and again with a PL singlet but with a 35 meV-blueshift ($E_0 \sim 6.08$ eV).

Figure 5. Statistical distribution of the PL energy E_0 extracted from spatially-resolved measurements performed at different excitation energies ($E_{ex} = 6.325$ eV). Each event in the histograms is weighted by the corresponding PL amplitude $\mathcal{A}_{PL}$.

Such a difference is consistent with the bandgap variations of monolayer hBN depending on the underlying susbtrate [31]. The ratio of the Raman and PL amplitudes is of the same order as the one estimated in figure 4 ($\mathcal{A}_R/\mathcal{A}_{PL} \sim 6$). This means that the optical response of exfoliated monolayer hBN in [15] is also determined by the interplay between resonant Raman

scattering and PL. This conclusion may be surprising considering the full suppression of the signal above 6 eV in the multilayer region of the exfoliated flake in [15]. While such phenomenology is straightforward for the PL component because of the direct-indirect crossover of the bandgap, one would expect to still detect some second-order Raman scattering in multilayer hBN. This is not the case because the resonance conditions enhancing the efficiency of the Raman processes are no longer satisfied when moving from monolayer to multilayer hBN. This effect is a second consequence of the drastic modification of the excitonic properties as soon as at least two monolayers are stacked in the hBN crystal [3–5]. First, the interlayer coupling slightly modifies the electronic band-structure and the nature of the bandgap, in particular with the conduction band minimum located at the *M* point of the Brillouin zone for multilayer hBN instead of the *K* point for monolayer hBN [3–5]. Second, the absorption of the excited excitonic states experiences a shift as large as $\sim$200 meV from one to two monolayers [5], which affects the resonant conditions of Raman scattering. This is why the resonant Raman scattering component of the UV-C emission vanishes together with the PL at $\sim$6.08 eV as soon as the hBN crystal consists of more than one monolayer in [15].

We have reported hyperspectral imaging in the UV-C spectral domain in epitaxial monolayers of hBN grown by HT-MBE on a HOPG substrate. We have shown that the UV-C emission of monolayer hBN consists in resonant Raman scattering and PL, which appear to be spatially uncorrelated. Systematic measurements as a function of the quasi-resonant laser energy unveil a PL singlet at $\sim$6.045 eV with spatial variations of the PL energy of $\sim$10 meV. This inhomogeneous broadening is lower than the average PL linewidth of $\sim$25 meV, a value close to the radiative limit in monolayer hBN. Our methodology provides an accurate framework for assessing the opto-electronic properties of hBN in the prospect of scalable hBN-based devices fabricated by epitaxy.

Data availability statement

All data that support the findings of this study are included within the article (and any supplementary files).

Acknowledgments

ORCID iDs

J Bradford ⬡ https://orcid.org/0000-0003-2356-5816
T S S James ⬡ https://orcid.org/0000-0002-9681-1558
C J Mellor ⬡ https://orcid.org/0000-0001-5987-7876
P H Beton ⬡ https://orcid.org/0000-0002-2120-8033
S V Novikov ⬡ https://orcid.org/0000-0002-3725-2565
B Gil ⬡ https://orcid.org/0000-0002-1588-887X
G Cassabois ⬡ https://orcid.org/0000-0001-5997-4609

References

[1] Geim A K and Grigorieva I V 2013 *Nature* **499** 7459
[2] Caldwell J, Aharonovich I, Cassabois G, Edgar J H, Gil B and Basov D N 2019 *Nat. Rev. Mater.* **4** 8
[3] Blase X, Rubio A, Louie S G and Cohen M L 1995 *Phys. Rev. B* **51** 6868
[4] Wickramaratne D, Weston L and Van de Walle C G 2018 *J. Phys. Chem. C* **122** 25524
[5] Paleari F, Galvani T, Amara H, Ducastelle F, Molina-Sánchez A and Wirtz L 2018 *2D Mater.* **5** 045017
[6] Cassabois G, Valvin P and Gil B 2016 *Nat. Photon.* **10** 262
[7] Vuong T Q P, Cassabois G, Valvin P, Jacques V, Van Der Lee A, Zobelli A, Watanabe K, Taniguchi T and Gil B 2017 *2D Mater.* **4** 011004
[8] Vuong T Q P, Cassabois G, Valvin P, Jacques V, Cuscó R, Artús L and Gil B 2017 *Phys. Rev. B* **95** 045207
[9] Vuong T Q P, Liu S, Van der Lee A, Cuscó R, Artús L, Michel T, Valvin P, Edgar J H, Cassabois G and Gil B 2018 *Nat. Mater.* **17** 152
[10] Elias C *et al* 2021 *Phys. Rev. Lett.* **127** 137401
[11] Schuster R, Habenicht C, Ahmad M, Knupfer M and Büchner B 2018 *Phys. Rev. B* **97** 041201
[12] Mak K F, Lee C, Hone J, Shan J and Heinz T F 2010 *Phys. Rev. Lett.* **105** 136805
[13] Splendiani A, Sun L, Zhang Y, Li T, Kim J, Chim C Y, Galli G and Wang F 2010 *Nano Lett.* **10** 1271
[14] Elias C *et al* 2019 *Nat. Commun.* **10** 2639
[15] Rousseau A *et al* 2021 *Nano Lett.* **21** 23
[16] Valvin P, Pelini T, Cassabois G, Zobelli A, Li J, Edgar J H and Gil B 2020 *AIP Adv.* **10** 075025
[17] Schué L, Berini B, Betz A C, Plaçais B, Ducastelle F, Barjon J and Loiseau A 2016 *Nanoscale* **8** 6986
[18] Shima K, Cheng T S, Mellor C J, Beton P H, Elias C, Valvin P, Gil B, Cassabois G, Novikov S V and Chichibu S F 2024 *Sci. Rep.* **14** 169
[19] Wirtz L, Marini A and Rubio A 2006 *Phys. Rev. Lett.* **96** 126104
[20] Román R J P *et al* 2021 *2D Mater.* **8** 044001
[21] Chow C M, Yu H, Jones A M, Schaibley J R, Koehler M, Mandrus D G, Merlin R, Yao W and Xu X 2017 *npj 2D Mater. Appl.* **1** 33
[22] Wang P *et al* 2022 *Adv. Mater.* **34** 2201387
[23] Cassabois G *et al* 2022 *Phys. Rev. X* **12** 011057
[24] Cheng T S, Summerfield A, Mellor C J, Khlobystov A N, Eaves L, Foxon C T, Beton P H and Novikov S V 2018 *Materials* **11** 1119
[25] Wrigley J *et al* 2021 *2D Mater.* **8** 034001
[26] Nečas D and Klapetek P 2012 *Cent. Eur. J. Phys.* **10** 181
[27] Bourrellier R *et al* 2014 *ACS Photonics* **1** 857
[28] Cassabois G, Valvin P and Gil B 2016 *Phys. Rev. B* **93** 035207
[29] Klingshirn C F 2007 *Semiconductor Optics* (Springer)
[30] Reich S, Ferrari A C, Arenal R, Loiseau A, Bello I and Robertson J 2005 *Phys. Rev. B* **71** 205201
[31] Guo C, Xu J and Ping Y 2021 *J. Phys.: Condens. Matter* **33** 234001